Acta Astronautica 223 (2024) 25–35

Contents lists available at ScienceDirect

Acta Astronautica

journal homepage: www.elsevier.com/locate/actaastro

Research paper

SPRISS: Scalable and precise resistive impact sensor for smallsats, architecture description and tests

Samuele Enzo [a,*], Giacomo Battaglia [b], Federico Basana [a], Francesca Filippini [b], Monica Mozzato [b], Federico Marin [b], Luca Lion [a], Lorenzo Olivieri [c], Carlo Bettanini [c], Alessandro Francesconi [c]

[a] Centre of Studies and Activities for Space (CISAS) "Giuseppe Colombo", University of Padova, via Venezia, 15, Padova, 35131, Italy
[b] University of Padova, via 8 Febbraio, 2, Padova, 35122, Italy
[c] Department of Industrial Engineering, University of Padova, via Venezia, 1, Padova, 35131, Italy

ARTICLE INFO

Keywords:
Space debris
In-situ measurement
CubeSat
Impact sensor

ABSTRACT

Space debris are a tangible risk for satellites in Earth orbits. Indeed, in the last decades fragmentation events have generated a large number of uncontrolled objects that have made the debris population grow. Modelling the space debris environment is becoming a fundamental task to evaluate the vulnerability of operational satellites, the probability of accidental collisions with uncontrolled objects, and the evolution of the debris population. With this aim, remote and in-situ measurements provide valuable data to tune the space debris population models and improve their reliability. While large satellites can be observed and tracked from ground, the sub-millimeter debris population requires in-situ measurements. In this context, in-orbit impact sensors are a key technology to obtain information about the sub-mm space debris environment. In this framework, a small-scale impact sensor sized to be integrated in a 2U CubeSat is being developed at the University of Padova. The sensor consists of a multitude of thin, conductive stripes arranged on a thin film of non-conductive material. When a debris hits the sensor, one or more stripes are severed, and the impact is detected. Moreover, the sensor design ensures low power consumption, making it feasible for CubeSat space missions. This work presents the latest outcomes obtained from the development of the sensor. Specifically, structural analyses are performed to assess that the sensor can withstand the launch loads, as well as thermal analyses to confirm its endurance capability with in-orbit temperatures. The number of expected impacts during the mission is predicted through orbital propagation, using state-of-the-art debris environment modelling tools. Finally, the paper presents a functional shooting test and vibration tests, executed onto a development model of the sensor, which verify its functionality and validate a Technology Readiness Level (TRL) of 4.

1. Introduction

Space debris currently represent a risk for the safe and affordable exploitation of the Near-Earth orbits [1]. They are expected to further increase in the close future [2] reducing the accessibility to space for the next generations [3]. The scientific community is also concerned by the increasing number of large constellations [4,5] and small satellites [6,7] proposed and launched in already crowded orbits. To address the space debris issue, different solutions are under evaluation by the involved stakeholders, spanning from the definition of stringent regulations [8,9] and guidelines [10] to the evaluation of Active Debris Removal solutions [11–14] and missions [15,16] to transfer or dispose of the most dangerous uncontrolled objects currently in orbit and which fragmentation might compromise entire orbital shells [17–19]. Additional activities include the continuous monitoring of operational satellites and space debris in the context of Space Surveillance and Tracking [20,21] and Space Situational Awareness [22,23]. It shall be underlined that objects visible from ground are catalogued and continuously tracked and can be escaped by vehicles with propulsion capabilities through Collision Avoidance Manoeuvres [24,25]. However, smaller debris cannot be detected but they might still cause critical damages on operational satellites [26] such as the failure of parts or subsystems [27,28], up to the complete loss of the spacecraft [29,30]. In this context, the evaluation and modelling of the small-size (i.e., not trackable) space debris is becoming important to understand its effect both on satellites vulnerability and on the evolution and degradation of the space environment. In particular, current fragmentation and environmental models are often based on limited information and large uncertainties can be expected; for this reason,

* Corresponding author.
E-mail address: samuele.enzo@phd.unipd.it (S. Enzo).

https://doi.org/10.1016/j.actaastro.2024.06.033
Received 29 March 2024; Received in revised form 16 May 2024; Accepted 18 June 2024
Available online 29 June 2024

List of abbreviations

ADC	Analog to Digital Converter
ASD	Acceleration Spectral Density
BBM	BreadBoard Model
CDS	CubeSat Design Specification
COTS	Commercial Off-The-Shelf
CSKB	CubeSat Kit Bus
DM	Development Model
DUT	Device Under Test
EPS	Electrical Power System
EQM	Equivalent Qualification Model
FDIR	Fault Detection, Isolation and Recovery
FM	Flight Model
FOS	Factor Of Safety
GEVS	General Environmental Verification Standard
IS-SA	Impact Sensor Sensitive Assembly
IS-CB	Impact Sensor Control Board
IS-SP	Impact Sensor Support Plate
IS-DET	Impact Sensor Detector
LEO	Low Earth Orbit
LTAN	Local Time of Ascending Node
MCU	MicroController Unit
MOS	Margin Of Safety
OBC	On Board Computer
PCB	Printed Circuit Board
PSD	Power Spectral Density
PTFE	Polytetrafluoroethylene
SPI	Serial Peripheral Interface
SSO	Sun Synchronous Orbit
TRL	Technology Readiness Level
UART	Universal Asynchronous Receiver-Transmitter
WCC	Worst Cold Case
WHC	Worst Hot Case

more accurate and up-to-date observation data is required to correct and update such models.

Different technologies are being utilized to develop various sensors for in-situ measurements such as LAREDO [31], DENTS [32] and SBOC [33]. In addition, the surfaces of the satellite returned to ground, such as the solar arrays of the Hubble Space Telescope, can be used to validate the space-debris flux model [34]. In the last decade, some payloads were launched, for example, the "in-situ micro-debris measurement system" from JAXA aimed at detecting an impact with a space debris greater than 100 μm by assessing the integrity of thin and conductive stripes made of copper that are severed by an impact [35,36]. The Space Debris Sensor is a NASA experiment and it was launched in 2017 to record the time and scale of impacts from space debris using dual-layer thin films, an acoustic sensor system, a resistive grid sensor system, and a sensored-embedded backstop [37]. Some CubeSat-sized payloads with the objective of counting the impacts with sub-mm space debris have been proposed and launched. The ESA "Debris inOrbit Evaluator" (DEBIE-1) [38] is based on plasma detectors and piezoelectric transducers to measure the plasma generated by an impact, together with the momentum exchanged and the penetration of a thin aluminum foil. Another experiment was the Piezoelectric Dust Detector launched onboard the Armadillo mission to measure sub-mm space debris. It was based on a two ionized mesh grid and a piezoelectric element and has the aim of measuring the velocity, impulse, and time of each impact, providing information about mass, size and frequency of occurrence [39]. On the other hand, the SOLID payload employs CubeSat solar panels for in-situ space debris detection (100 μm size) [40].

With respect to the previous missions, the proposed sensor employs only resistive stripes printed on a thin film of non-conductive material. Moreover, it is miniaturized to be hosted on a 2U CubeSat face, but its design enables easy scaling and installation in a wide range of spacecrafts. The minimum detectable diameter of an impact is reduced to 80 μm. The method used for the reading of the conductive lines permits to simplify the electronic circuitry while reducing the power consumption with respect to the CubeSat-sized impact sensors proposed in the literature. The sensor is developed in the framework of the AlbaSat mission [41]: a 2U CubeSat that is expected to be launched in a 500 km Sun Synchronous Orbit (SSO) in 2027. This altitude is a constraint derived from the ESSB-ST-U-007 in which it is required that a spacecraft without propulsion re-entries in the atmosphere within 5 years from the start of the mission. AlbaSat will provide the opportunity to test the sensor in space but, since gaining information about the sub-mm space debris environment in more crowded orbits is crucial, the employment of the sensor in higher orbits in future is considered. Indeed, a single CubeSat mission is not sufficient to acquire a statistically significant amount of data to improve the reliability of debris models. Hence, the primary objective of the current study is to develop a scalable sensor capable of detecting impacts with space debris in orbit. This will provide a tool that can be used by different future missions to collect data on the sub-mm space debris environment.

In [42], the first phases of the design of the sensor are presented. The research work contains a description of the sensor from a physical and functional point of view, a brief discussion about mission feasibility, and a presentation of the BreadBoard Model (BBM), which brought the technology to a TRL of 3. All aforementioned subjects have been updated and are also explained in an extensive way in this paper, respectively in Section 2, and Section 3.1. In Section 3.1, more refined environmental analyses are shown with respect to [42], which bring to the same conclusions about mission feasibility and the need of this kind of sensor. Concerning the BBM, it was composed of an Arduino Uno as processing unit, and COTS electrical components to form the control circuit (multiplexers, demultiplexers and diodes), everything connected on a breadboard. Debris detection was represented by manual switches. Despite its simplicity, its representativeness was compliant to verify the functional architecture of the sensor, the software algorithm and the control electronics circuit.

This paper presents the consolidated design obtained from the development of the BBM with particular focus to the analyses performed to verify the functionality of the sensor in orbit and the test campaign performed to validate the payload. The paper is organized as follows: Section 2 presents the physical and functional architecture and the structure of the flight software; Section 3 shows the numerical analyses, i.e., impact probability, thermal and structural analyses, performed for verifying the sensor; Section 4 presents the test campaign conducted on the sensor i.e., functional shot test and vibration test, and provide the results; in Section 5 conclusions are drawn.

2. Sensor architecture

The sensor aims at detecting impacts with sub-millimeter debris in Low Earth Orbit (LEO). In the followings, the physical and functional architectures are presented together with the software structure.

2.1. Physical architecture

The design of the sensor is driven by the Size, Weight and Power (SWaP) constraints that a 2U CubeSat platform imposes. In fact, according to the CubeSat standard, no components on the lateral faces of the satellite (approximately 10 × 20 cm) shall protrude farther than 6.5 mm normal to the surface from the plane of the rail. In addition, the size of the solar panels determines how much power can be generated

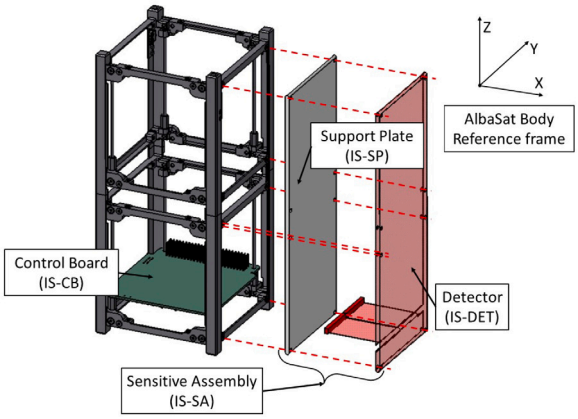

Fig. 1. CAD representation of the sensor assembly. The detector (IS-DET) wraps the support plate (IS-SP). The horizontal plate represented between IS-DET and IS-SP is the connection band that allows the communication between the sensitive lines and the control board (IS-CB). (For interpretation of the references to colour in this figure legend, the reader is referred to the web version of this article.)

Table 1
Mass estimation of the components.

Component	Mass (g)
IS-SP	117
IS-CB	60
IS-DET	17
Total	194
Total + 20%	**233**

onboard. Because the CubeSat standard requires a specific size of 10 × 10 × 20 cm for a 2U CubeSat, the amount of power generated onboard, especially with solar panels mounted on the body, is limited as a result. Hence, the sensor is designed to have a power consumption lower than 0.5 W. Another design driver is the scalability of the sensor. In fact, the philosophy behind the CubeSat standard is founded on the possibility of making satellites of variable dimensions by stacking basic building blocks. The scalability and the conformity with the CubeSat standard allow to employ the sensor on different missions configurations, allowing to collect more information about the sub-mm space debris environment.

The developed sensor consists of three main components: (1) a detector (IS-DET), (2) a support plate (IS-SP), and (3) a control board (IS-CB). Fig. 1 provides a representation of the sensor and the mass estimation of the components is reported in Table 1. The IS-DET is the sensitive part of the sensor. It consists of a flexible Printed Circuit Board (Printed Circuit Board (PCB)) featuring a series of conductive lines, each 80 μm wide, arranged in parallel and spaced 80 μm apart. These two parameters were chosen as a trade-off between the manufacturing limits of flexible PCB technology, production costs, and the sensor resolution requirements. Specifically, the production costs increase dramatically when approaching the technological limit. As the current sensor is intended for use in CubeSat missions, a slight increase in resolution of a few micrometres does not justify the significant increase in cost. The conductive stripes are printed on a 50 μm thick Kapton film that protect them from the space environment. In fact, in order to detect an impact with a space debris, the conductive stripes must be exposed to the outer space. If an impact occurs, the IS-DET is perforated and one or more lines severed. The sensor is capable of detecting craters originated by an impact with a minimum diameter of 80 μm. The IS-DET is attached with a space-graded bounding tape (3M 9460) to the IS-SP, a 3 mm thick Polytetrafluoroethylene (PTFE) plate. This has two functions: (1) to provide structural rigidity to the IS-DET and (2) to shield the internal components of the satellite from the impact with a

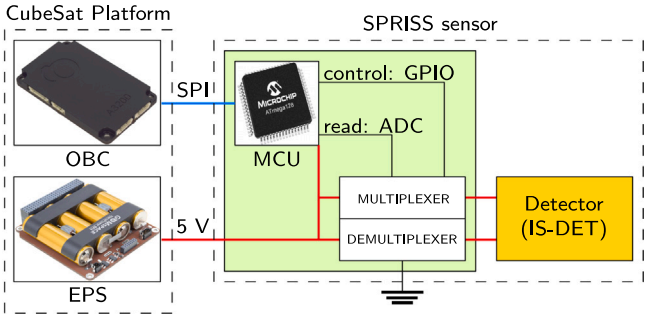

Fig. 2. Functional diagram of the sensor.

space debris. The assembly formed by the IS-DET and the IS-SP is called Sensitive Assembly (IS-SA). As shown in Fig. 1, the IS-SA is secured with 8 screws to the face of the CubeSat that points towards the velocity direction of the satellite to maximize the probability of measuring an impact. The screws utilize the CubeSat structure existing holes, originally intended for mounting solar panels. The IS-DET is connected to the IS-CB through a connector band part of the IS-DET itself. The IS-CB respect the PC104 standard and is integrated in the satellite. It contains the control electronics required for the reading of the IS-DET such as microprocessor, multiplexer, demultiplexer. Specifically, the microprocessor is an Atmega128 since its rad-hard version is available as Commercial Off-The-Shelf (COTS) component.

To mitigate the effect of the space environment on the sensor, the flight model of the IS-DET and of the IS-SP will be coated in a thin layer of Indium Tin Oxide (ITO). This coating will add a negligible thickness to the components, around 0.25 μm, but will help to mitigate the effect of differential charging on the satellite [43]. In fact, the coating is conductive and will be grounded to the structure of the CubeSat through the same bolts that hold the IS-SP in place. At the same time, the coating will help limiting the erosion caused by the action of the atomic oxygen on the Kapton film [44].

2.2. Functional architecture

A space debris impacting with the sensor perforates the detector, severing one or more conductive stripes. Hence, by reading the electrical conductivity of the lines it is possible to detect the impact: a severed line acts as an open electrical circuit preventing the transmission of a signal.

Fig. 2 shows the functional diagram of the system. The IS-CB reads the lines state by looping through them, stores the data and transmits them to the On Board Computer (OBC) through a Serial Peripheral Interface (SPI) connection. The IS-CB is connected with the CubeSat bus, that provides electric power supply from the Electrical Power System (EPS). Inside the IS-CB, a MicroController Unit (MCU) manages the reading process, by taking advantage of a multiplexer/demultiplexer electronic architecture, which enables unique identification of the lines and multiplication of the signal, consistently reducing the number of inputs needed in the IS-CB.

Each line is connected to a multiplexer on one side and to a demultiplexer on the other as shown in Fig. 3. Each multiplexer channel is connected to n consecutive lines, and each demultiplexer channel is connected to n lines, each one coming from a different multiplexer. This connection layout, using a 1: n multiplexer and a n: 1 demultiplexer, allows the control of n^2 lines. Blocking diodes are placed to allow the selection of a single line by the control circuit. In this way, each line is identified by a unique ID, corresponding to the multiplexer/demultiplexer channel to which it is connected. For instance, in a configuration with $n = 4$, there will be 16 available lines, identified by combinations of the channels for the multiplexer/demultiplexer.

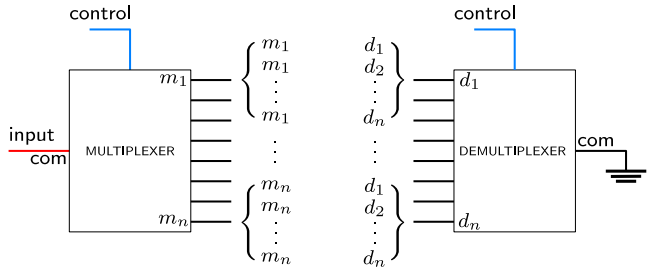

Fig. 3. Circuitry representation of the sensor. Each multiplexer channel is connected to a different demultiplexer channel, allowing to detect a maximum of n^2 strips. The com signal of the multiplexer goes into the input ADC, and it is read thanks to the pull-up resistance. The com signal of the demultiplexer is connected to ground. Blocking diodes are present for each strip (not represented).

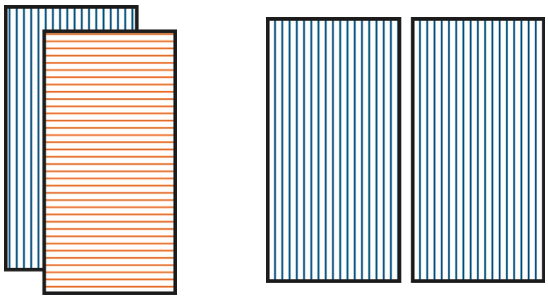

Fig. 4. Conceptual representation of the re-scaled solutions for IS-DET. On the left side, a two-layer configuration is presented. On the right side, two IS-DET building blocks are placed side by side to increase the total sensitive area.

In this example, channels from the multiplexer and the demultiplexer are $(0, 1, 2, 3)$, and consequently the lines IDs will be respectively $0/0$, $0/1$, $0/2$, $0/3$, $1/0$, $\ldots$, $3/3$. When a stripe is selected, it is connected to the input port on the MCU and to ground, and a pull-up resistor enables deterministic read of the line state (open, i.e., broken, or closed, i.e., intact).

The IS-DET employs 440 sensible lines. Multiplexer/ demultiplexer channels are employed for verification purposes, i.e., checking the overall well-being of the device in flight. The presence of an "always open" and an "always closed" line enables fast sanity checks of the whole detection chain. A reduced model is employed for the purposes of the test campaign presented in this work, as described in Section 4.1.

2.3. Software architecture

Since the MCU is an Atmega128, an Arduino-style code is written using the MegaCore library.

The MCU is connected to the OBC through an SPI interface. Additionally, the software features a Universal Asynchronous Receiver-Transmitter (UART) interface for debugging purposes. The choice of the Arduino environment is motivated by the fast prototyping and low-cost design of the software logic.

The software architecture employs two main routines: a lines detection loop and a command parser. Other routines such as memory checking and safety routines for Fault Detection, Isolation and Recovery (FDIR) will be added in future versions of the software. The command parsing routine is a standard ID + arguments format, stored in a buffer and passed to parsing functions which trigger specific actions in a pre-defined command library.

The core of the software is the lines detection routine. Its aim is to update the lines status saved in memory by means of successive reads, obtained by constantly looping through the IS-DET lines. They are identified with unique IDs as explained in Section 2.2. Each line is selected by looping through the channels of the multiplexer/demultiplexer couples. Two loops are nested in this routine. A slower loop selects the multiplexer channel to check, and a faster loop scans through all the demultiplexer channels to measure the state of each adjacent line consecutively. The line state is determined though a voltage read by the Analog to Digital Converter (ADC), and it is stored as a bit in memory: 1 for "open", and 0 for "closed". The lines status is efficiently stored in memory as a binary word, where each bit corresponds to a single line. The sampling rate of each line is set to 1 Hz allowing the temporal identification of an impact. Moreover, if the IS-DET state changes, i.e., a line has been broken, the software sends a notification to the OBC and prepares to dump the lines status.

Overall, the software is designed to work alongside the on-board software, aiming to be controlled by the OBC as a peripheral unit in the system.

2.4. Sensor scalability

The sensor concept is based on scalability. This is a fundamental point, as bigger sensors of this kind will be needed for future extensive in-situ measurement missions. The simplicity and modularity of this design allow for easy re-sizing. Moreover, its low impact on power and data budgets also aid its implementation on multi-purpose missions.

Scalability applies to all components of the sensor assembly. Using the same reference frame as Fig. 1, the IS-DET can be re-sized both in Y-axis and Z-axis directions. Along the Y-axis it is sufficient to increase the number of conductive stripes, while along the Z-axis the length of the stripes can be increased. To have more information about debris impact location, an orthogonal set of stripes can be adopted. This architecture allows a more reliable detection of multiple impacts improving lines redundancy. Moreover, multiple IS-DET building blocks could be stacked in a grid-like style increasing the sensitive area. Fig. 4 shows a conceptual representation of the two rescaling approaches.

Scalability also extends to the control circuitry. In fact, it only reflects on the number and type of multiplexer/demultiplexer couples which are used for the design. This could affect the space requirements in the IS-CB, but this remains in any case negligible compared to the surface occupied by the IS-DET. Connections between the two parts of the assembly are highly application dependent: the design employed for this CubeSat application might be reviewed for bigger instalments of this technology. From the IS-CB computational power point of view, it would still not be an issue for bigger systems, as precise time-tagged detection is not usually needed for these applications, so the detection cycle might also be brought to a lower rate.

Because of these considerations, this sensor design proves high flexibility. Applications on bigger scale missions, as a feature of a multi-payload system, are going to be further explored after mission demonstration success.

3. Numerical analysis

This section presents the numerical analyses conducted to verify the functionality of the sensor in orbit. Firstly, an analysis of the number of impacts that may be collected during the mission is presented. Subsequently, the thermal and structural analyses of the behaviour of the sensor during the AlbaSat mission are shown.

3.1. Debris analysis

In order to determine the number of impacts that the sensor may detect, an analysis is conducted employing the Debris module of the Systema software. Only the sensitive part of the sensor is considered in these simulations and it is modelled as a 3 mm PTFE (Teflon) plate covered by a thin layer of copper (27 μm) pointing towards velocity in a SSO. The starting date is considered equal to the AlbaSat mission (March 2027) and the period considered in the analysis is one year,

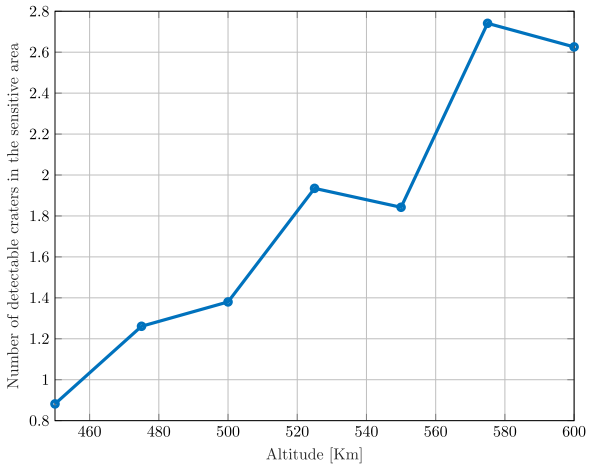

Fig. 5. Number of detectable impacts considering a sensitive area of 0.018 m^2 for different altitudes in the case of 1 year mission starting from March 2027. An impact is considered detectable if the crater on the IS-SA has a depth greater than the thickness of the sensitive copper layer (27 μm).

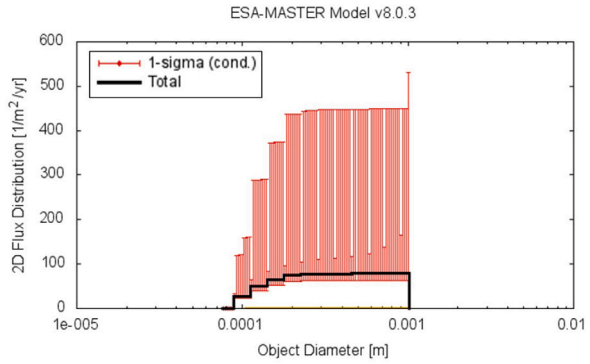

Fig. 6. The graph shows the 2D flux distribution (black line) versus the debris diameter predicted by the ESA MASTER Model. The red vertical lines represent the 1-sigma uncertainty of the model. The uncertainties are strongly asymmetrical, indicating that within the sub-millimeter debris population range, the flux can be approximately 4 or 5 times higher than expected. (For interpretation of the references to colour in this figure legend, the reader is referred to the web version of this article.)

equal to the expected operative life of the satellite. The debris population is extrapolated from ESA MASTER software considering the future condensed populations (years from 2026 to 2029) and meteoroids. Condensed populations include all the single source contributions of space debris excluding meteoroids in a single source allowing to increase the processing speeds of the simulations [45]. Only craters with a diameter larger than the sensor resolution limit (80 μm) and a depth greater than the thickness of the copper layer are considered as detectable impacts. Therefore, an impact is considered detectable if the debris penetrates the outer layer of the IS-DET and creates a crater on the IS-SP.

The results are depicted in Fig. 5. The number of detectable impacts on the sensitive area of the sensor (0.018 m^2) varies from 0.88 at 450 km to 2.74 at 575 km considering 1 year of operative life. Considered these results, the probability of multiple impacts within the same sensitive line is low. Therefore, this issue is not considered critical for the design of the sensor.

The predictions obtained are underestimated due to the significant uncertainties affecting the numerical models. Fig. 6, derived from [42], allows to visualize the 2D flux of space debris in the range of 1-1000 μm predicted by the ESA-MASTER Model for the AlbaSat mission at an altitude of 500 km. The 1-sigma uncertainty bars of the model are shown in red and their asymmetry indicates that the flux can be approximately 4 or 5 times higher than calculated and, as a consequence, the actual number of detectable impacts could be higher. Furthermore, future fragmentation events in LEO could contribute to an increase in the density of the debris population in orbit [2].

Table 2
Orbital parameters for thermal analyses.

	Dawn-Dusk orbit	Midday-Midnight orbit
Altitude	500 km	500 km
Eccentricity	0.001	0.001
LTAN	06:00	12:00
Epoch	30/03/2027	30/03/2027

Table 3
Electrical Power Consumption.

Orbit	Mode	IS-CB	Other subsystems
Dawn-Dusk	Nominal	0.3 W	4.804 W
	Safe	0 W	1.036 W
Midday-Midnight	Nominal	0.3 W	2.407 W
	Safe	0 W	1.036 W

3.2. Thermal analysis

Numerical analyses are performed to evaluate the thermal behaviour of the sensor during the AlbaSat mission. Both the IS-SA and the IS-CB are investigated under various orbital scenarios (Table 2) and during the two most critical modes for the AlbaSat mission from the thermal standpoint: Nominal Mode (Worst Hot Case, WHC) and Safe Mode (Worst Cold Case, WCC) [41]. In the simulations, the 2U CubeSat is modelled using Systema Thermica module to depict conductive and radiative heat exchanges. The sensor is modelled as being fixed to the CubeSat structure under flight conditions. All of the subsystems are representative of the Flight Model (FM) of the AlbaSat mission [41]. "The assembly IS-DET–IS-SP is represented as a three-layered plate (Kapton - PTFE - Kapton), with the middle layer corresponding to the IS-SP and the other two layers representing the IS-DET and the physical connections with the IS-CB. These latter two layers were modelled using copper material for the IS-SP core and Kapton as a surface covering. The IS-CB is modelled as a single plate made of FR4 connected to the IS-DET.

Concerning orbital scenarios, the two extreme conditions for the AlbaSat SSO are taken into consideration: the Dawn-Dusk orbit and the Midday-Midnight orbit. The first one represents the most challenging hot case due to the maximum duration of daylight, whereas the second one is the most critical cold case, as it experiences the maximum duration of the eclipse. The selected orbital parameters are reported in Table 2.

On the other hand, as reported in [41], the distinction between the Nominal Mode and the Safe Mode lies in the varying global electrical power requirements for the subsystems. As summarized in Table 3, the Nominal Mode demands the highest power value, leading to the maximum generation of dissipated heat. Conversely, the Safe Mode requires the minimum power, resulting in the least amount of dissipated heat generation.

In summary, the following four main scenarios have been identified and analysed:

— Dawn-Dusk orbit with the Nominal Mode activated (WHC);
— Dawn-Dusk orbit with the Safe Mode activated;
— Midday-Midnight orbit with the Nominal Mode activated;
— Midday-Midnight orbit with the Safe Mode activated (WCC).

Figs. 7 and 8 show the temperature profiles for the outer surface of the IS-SA and the IS-CB respectively, for the four scenarios. The decision to present results just from the outer layer of the IS-SA is due to the observation that, throughout the Dawn-Dusk orbit, all three layers show a similar temperature transient evolvement, with a difference of

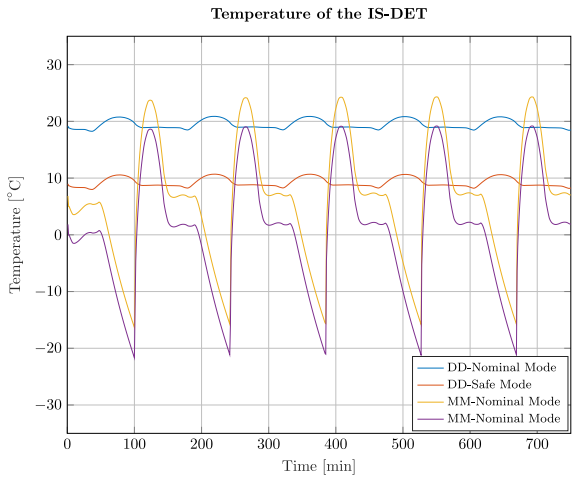

Fig. 7. Temperatures of external layer of IS-DET.

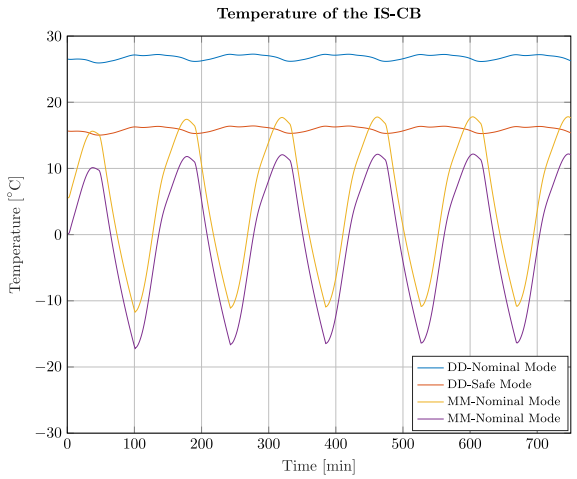

Fig. 8. Temperatures of IS-CB.

Table 4
Maximum and minimum temperatures obtained from thermal analyses.

Orbit	Mode	IS-DET [°C]		IS-CB [°C]	
		T_{Max}	T_{Min}	T_{Max}	T_{Min}
D-D	Nominal	+35.76	+3.31	+42.17	+11.03
	Safe	+25.57	−6.95	+31.32	+0.12
M-M	Nominal	+39.37	−30.70	+32.83	−25.89
	Safe	+34.27	−36.08	+27.21	−31.41

Table 5
Comparison between the calculated temperatures (Analysis) and the limit operative temperatures of the electronic components (Limit).

	Max Temp. [°C]		Min Temp. [°C]	
	Analysis	Limit	Analysis	Limit
IS-SA	+39.37	+125.00	−36.08	−40.00
IS-CB	+42.17	+105.00	−31.41	−55.00

at most 5 °C. In contrast, during the Midday-Midnight orbit, the outer layer experiences the most significant temperature gradient. Hence, it was chosen to represent the results focusing on this specific layer.

Table 4 reports results incorporate uncertainties of ±15 °C, according to ECSS-E-HB-31-03 A [46]. In the Dawn-Dusk orbit temperatures are not affected, with minimal fluctuations due to consistent lighting conditions. On the other hand, the Midday-Midnight orbit presents significant temperature variations between the maximum and minimum values. This gap is associated with the occurrence of approximately 34 minutes of eclipse during each orbit. Examining both the WCC and the WHC, it is demonstrated that the temperatures of the IS-SA and IS-CB, as determined by the analyses, fall within the operational temperature range specified for their electronic components, as illustrated in Table 5.

Table 6
Material properties used in simulations.

Property	PTFE	Flex PCB	FR4
Density [$\frac{kg}{m^3}$]	2245.1	1420	1900
Young's modulus [GPa]	0.39	1.5	22
Poisson's ratio [−]	0.45	0.34	0.14
Yield strength [MPa]	20.7	69	200
Ultimate strength [MPa]	26.7	200	320

3.3. Structural analysis

Structural analyses are conducted with ANSYS Mechanical. The two main components of the sensor, namely the IS-SA and the IS-CB, are studied in two dedicated analyses.

Moreover, a modal analysis is conducted to determine the resonance frequencies of the Development Model (DM) of the sensor having an associated effective mass higher than the 10% of the total mass.

The first analysis is dedicated to the IS-SA. It is simplified as a 3 mm plate made of PTFE (Teflon) to represent the IS-SP, and two 0.2 mm layers made of Kapton on the $\pm X_{BODY}$ faces to represent the IS-DET. A bonded contact is imposed between the IS-SP and IS-DET, in order to simulate the glued contact between these components. The assembly is fixed to the CubeSat structure by employing the eight threaded holes (red lines in Fig. 1) originally intended for mounting the solar panels. Hence, the boundary conditions impose a fixed joint constraint to each hole. The surfaces in contact between the IS-SA and the structure of the CubeSat are also fixed.

In the second analysis the IS-CB is considered. It is simplified as a plate made of FR4, having a total mass of 53.65 g. The IS-CB is fixed to the CubeSat secondary structure using four spacers that pass through four holes close to the vertices of the IS-CB. In addition, the PCB is connected to the CubeSat bus by means of a CubeSat Kit Bus (CSKB). Hence, the boundary conditions are: (1) a fixed joint constraint for each PC104 hole and (2) a fixed support on the area in contact with the CSKB.

Both the studied components are considered oriented as they would be in the flight model configuration. The main properties of the materials considered within the models are reported in Table 6.

Quasi-static and random vibration analyses are conducted to verify that the sensor withstands the applied loads from a launch vehicle. At the moment of writing this document, the launcher has not been identified and the following loads levels are assumed. For the quasi-static analysis is considered a worst-case of a 10 g load applied to each of the three Cartesian axes, as per VEGA-C User Manual [47]. For the random vibration analysis, the acceleration spectral density (ASD) profile at qualification level (in orange in Fig. 9) given by the General Environmental Verification Standard (GEVS) [48] is considered. According to the ECSS-E-ST-32-10C [49], this load profile is multiplied by a design factor. The obtained profile is applied to each of the three axes with a 3σ Gaussian probability distribution.

The design factor is the product of the following quantities:

— Model factor K_M: it considers the representativity of mathematical models;
— Project factor K_P: it takes into account the maturity of the design and its possible evolution and programmatic margins;

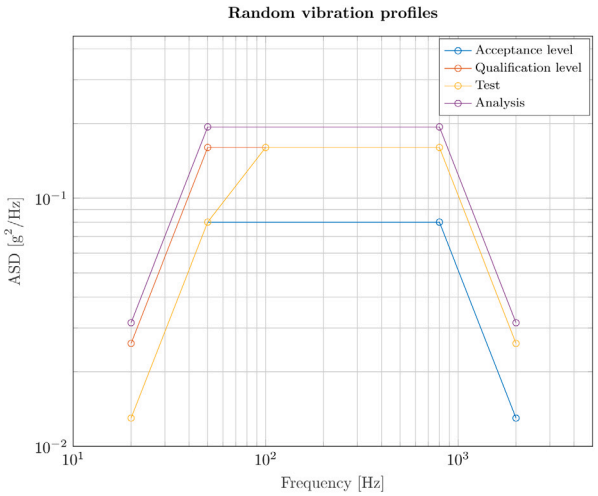

Fig. 9. Random vibrations profile at qualification level (orange) and acceptance level (blue), from GEVS [48]. The purple profile is the one applied in simulation. The yellow profile is the one used in the vibration tests in Section 4. (For interpretation of the references to colour in this figure legend, the reader is referred to the web version of this article.)

Table 7
Design factor, and factor of safety considered in this document.

	K_M	K_P	K_Q	FOS_y	FOS_u
Quasi-static	1.1	1.2	2	1.25	2
Random	1.1	1.1	/	1.25	2

— Qualification test factor K_Q: factor used to define the qualification test loads. In random vibrations analysis this factor is considered already included in the limit loads.

The values of the factors considered for the quasi-static and random vibration analyses are listed in Table 7. Therefore, the load utilized in random vibration simulations corresponds to the one depicted in Fig. 9 (purple line). On the other side, a 26.4 g load is applied for the quasi-static analysis.

In Table 8 are reported the maximum directional deformations that occurs for each of the three axes, considering the load applied in the same direction. Components deformations are considered not only to assess the occurrence of significant deformations that could potentially damage the components themselves but also to comply with requirement 2.2.3 from CubeSat Design Specification (CDS) Rev. 14.1 [50], which stipulates that components mounted on the sides of a CubeSat must not protrude more than 6.5 mm normal to the surface from the plane of the rail, even after the application of dynamic loads. The resulting directional deformations are all well below 1 mm, indicating that no major deformations occur on the components, thereby satisfying the mentioned requirement. For the IS-SA the most severe deformation occurs along the Y-axis when the random loads are applied along the Y-axis , whereas, for the IS-CB, it occurs along the Z-axis when the random loads are applied along the Z-axis.

For both the analyses, the worst-case configurations (i.e., the one with the most severe stress) are the ones with the loads applied in the Y-axis direction for the IS-SA, and in Z-axis direction for the IS-CB. The maximum equivalent stress occurred for each material is reported in Tables 9 and 10. From the two tables, it can be seen that random loads are the ones that provide the greatest stress on all components. In both cases the most severe stresses occur close to the bolted joints.

To verify that the components could withstand the design limit loads, the Margin of Safety (MOS) is calculated, according to ECSS-E-ST-32-10C [49], as:

$$MOS = \frac{Allowable\ strength}{Max\ calculated\ stress\ *\ FOS} - 1 \quad (1)$$

Table 8
Maximum deformations calculated in quasi-static and random vibrations analyses.

		Quasi-static deformation [mm]	Random deformation [mm]
IS-SA	X-axis	0.096	0.013
	Y-axis	0	0.11
	Z-axis	0	0.089
IS-CB	X-axis	0	0
	Y-axis	0	0
	Z-axis	−0.04	0.17

Table 9
Quasi-static analysis stress results.

	Material	Eq. stress [MPa]	MOS_y	MOS_u
IS-SA	PTFE	0.33	49.18	39.45
	Flex PCB	3.05	17.10	31.79
IS-CB	FR4	8.18	18.56	18.56

Table 10
Random vibration analysis stress results.

	Material	Eq. stress [MPa]	MOS_y	MOS_u
IS-SA	PTFE	3.64	3.55	2.67
	Flex PCB	34.1	0.62	2.67
IS-CB	FR4	34.9	3.58	3.58

A positive MOS indicates that the component can withstand the design limit loads.

The allowable strength considered in the formula is the value of ultimate and yield strength for all the materials involved in the simulations (Table 6), since these denote the lowest stresses at which failure and plastic deformation occur, respectively. For what concern the choice for the Factor of Safety (FOS), ECSS-E-ST-32-10C [49] defines the FOS for yield and ultimate strength that have to be used in simulations. The chosen FOS values are reported in Table 7. Therefore, using the maximum equivalent stresses for each component resulted from the quasi-static and random vibration analyses, two MOS (one for yield strength MOS_y, the other for ultimate strength MOS_u) for each material are calculated. The results are reported in Tables 8 and 10. It can be noted that all the MOS are positive thus, according to these analyses, every component withstand the applied design loads.

A modal analysis is performed to determine the resonance frequencies that have an associated effective mass higher than the 10%, to allow the validation of the success criteria of the vibration test described in Section 4.3. For that purpose, a dedicated model is used since the Device Under Test (DUT) is the DM as described in Section 4.1. The IS-SP is modelled as a 3 mm plate made of PTFE, and the IS-DET as a 0.2 mm surface of flex PCB applied on the +X-axis face. The glue between the two components is simulated as a bonded contact. The assembly is fixed to the interface by fixed joints constraint through the eight threaded holes as in-flight conditions (red lines in Fig. 1), and the -X-axis face is fully supported. To recreate this condition and to not risk to over-constrain the model, a compression only support is adopted. The results indicate that the only resonance with an associated effective mass exceeding 10% occurs at approximately 640 Hz. This value is used to identify the peak to be deeply analysed in the post processing phase of the resonance search test described in Section 4.3.

4. Test campaign

4.1. Device under test

The numerical analyses verified that the sensor withstands the launch loads and that the in-orbit temperatures do not exceed the operative temperatures of the components of the sensor. In order to

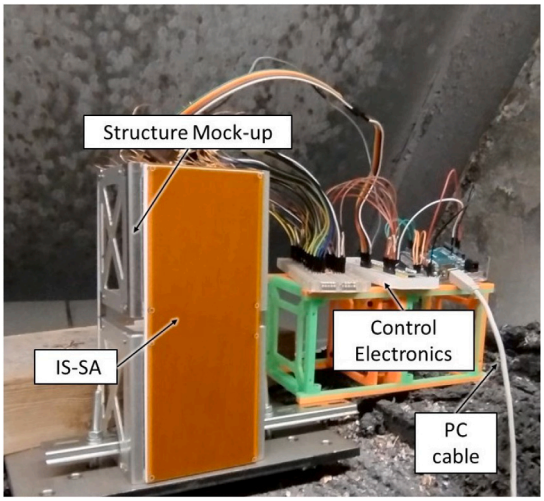

Fig. 10. Development Model of the sensor before the functional test at the shooting range, see Section 4.2. The detector is mounted on a mock-up of a 2U CubeSat and fixed to a heavy base plate in steel approximately 25 × 25 cm, 8 mm thickness, to provide stability. The control electronics are positioned at a sufficient distance to prevent accidental impacts.

assess its functionality, a reduced test campaign is performed on a Development Model (DM) of the sensor.

The DM is representative of interfaces, critical functionalities, materials and critical manufacturing processes of the FM of the sensor. The purpose of this model is to verify the assembly and interfaces of the IS-SA, the manufacturing limits of the flexible PCB technology, the capability of the sensor to detect an impact, and the capability of the IS-SA design to resist launch loads at the level described in Fig. 9 (random vibrations) and in Table 12 (sinusoidal vibrations). The test campaign performed to verify these goals is presented in this section. On the other hand, the control electronics and the cabling are not representative of the FM and therefore their only aim during the present test campaign is to allow the collection of data of the lines status.

The DM of the sensor (Fig. 10) is composed by a breadboard model of the control electronics, a simplified version of the IS-DET and a FM equivalent IS-SP. The IS-CB and the OBC are represented by an Arduino Uno and a PC respectively. As for the FM, the DM (Fig. 11) consists of a flexible PCB glued on a PTFE plate through a space graded bounding tape. The number of sensitive lines is reduced from 440 to 64 to simplify the design. The conductive lines of the DM are spaced of 80 µm and have a width of 80 µm. The lines are ordered to cover the same sensitive area of the FM. Indeed, while on the FM the lines are arranged in parallel, in the DM, the 64 lines follow a "S" pattern to cover the whole sensitive area of the FM. The diodes used in the reading circuit are the same but reduced in number (from 440 to 64) of the ones used in the FM. In this model, the dimensions and the interface holes of IS-DET and IS-SP are the same as the FM in order to verify the assembly procedure of the sensor to the CubeSat structure.

The DM is considered representative of the FM for what concerns: (1) the functionality of the sensor, (2) the mechanical response to a load of the IS-SA and (3) the mechanical interface of the IS-SA with the CubeSat. Hence, a test campaign is performed on it to assess its functionality and its behaviour under launch loads. Firstly, the test to verify the functionality of the sensor is conducted at the shooting range of Padova. Secondly, a vibration test at acceptance level is performed do confirm the capability of the IS-SA glued interface and its fixture system to the CubeSat to withstand the launch loads. A Technology Readiness Level (TRL) equal to 4 (Component and/or breadboard functional verification in laboratory environment [51]) is reached through these tests.

Fig. 11. Simplified detector design used for the Development Model of the sensor. The diodes are placed in the top-left edge of the board and the stack connector to the control electronics in the bottom-left edge. The 64 sensitive lines are arranged using an "S" pattern to cover the entire sensitive area.

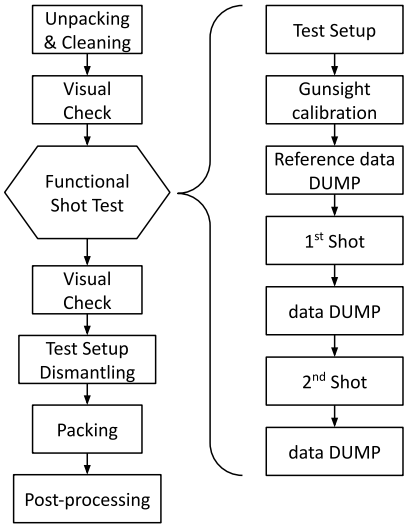

Fig. 12. Functional Shooting Test sequence followed for the test campaign. Two different shots have been executed.

4.2. Functional shooting test

The main objective of this test is to demonstrate the capability of the sensor to detect an impact in a laboratory environment. In particular, the sensor shall identify the severed lines and send the information to the OBC (represented by a PC).

The test procedure is described in Fig. 12. Initially, the DUT is unpacked, cleaned, and inspected to confirm its readiness for the test. Subsequently, the DUT is positioned on the target surface of the shooting range, and the Arduino Uno, embarking the sensor software, is connected to the PC through serial connection. A first data dump is performed to serve as a reference of the sensor status. Then, the gunsight is calibrated to ensure accurate shots can be taken. At this stage, the shooting procedure can take place, and each shot is followed by a data dump. All data is stored to facilitate the comparison of line status before and after each shot. A visual check is also conducted to verify the integrity of the back surface of the Support Plate. Finally, the test setup is dismantled and packed.

The Impact Sensor is mounted of an aluminum structure mock-up of a 2U CubeSat using the same physical interfaces of the FM described in Section 2.1. The breadboard representing the control electronics is placed next to the IS-SA at safe distance to prevent an accidental impact between the projectile and electronics components. Finally, the structure is secured to a steel plate to provide stability and the whole assembly is positioned on the target support of the shooting range, as depicted in Fig. 10.

To perform the test, an air rifle having an energy of 7.5 J is used. The main characteristics of the bullet are reported in Table 11. The

Table 11
Bullet characteristics.

Parameter	Value
Mass	0.483 ± 0.002 g
Diameter	4.5 mm
Velocity	~ 175 m/s

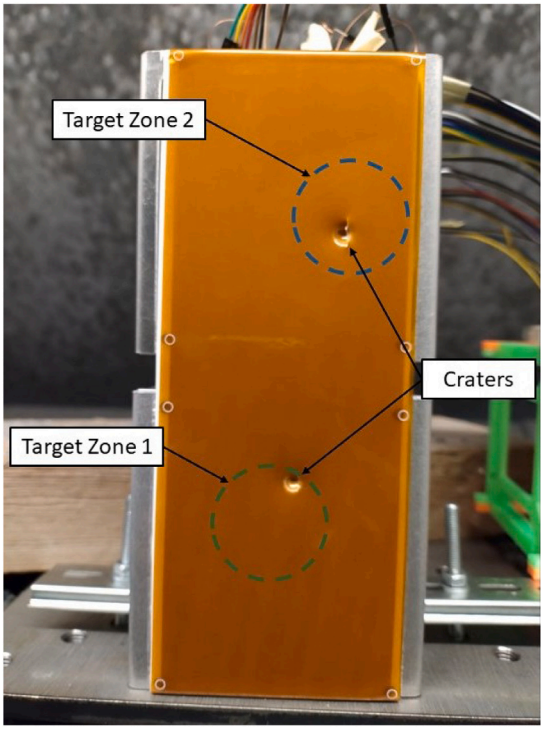

Fig. 13. The 1st target zone is located in the middle-right of the upper 1U face of the satellite, the 2nd one is located in the middle of the bottom 1U face. These zones were selected to have a higher probability to sever different lines. The craters generated by the impacts are visible and located inside the target zones.

velocity of the impact is lower than the velocity of an impact in LEO that can reach a value of $\sim 10\,\mathrm{km\,s^{-1}}$, and the diameter of the bullet exceeds the size of the particles the sensor is designed to detect. Nonetheless, the impacts conducted during the test can be deemed representative of a hypervelocity collision with a space debris in terms of energy. The kinetic energy E_k of the debris can be calculated using Eq. (2), where m and v represent the mass and velocity of the debris, respectively. Assuming the debris to be an aluminum sphere, its mass can be estimated using Eq. (3), where the density ρ equals $2700\,\mathrm{kg\,m^{-3}}$.

$$E_k = \frac{1}{2} m v^2 \tag{2}$$

$$m = \frac{1}{6} \rho \pi d^3 \tag{3}$$

By setting the value of E_k to 7.5 J and v to $10\,\mathrm{km\,s^{-1}}$, the diameter of the equivalent space debris is 0.47 mm, which falls within the dimensional range of sensitivity of the sensor.

Two different shots are performed with two different target zones of the detector, as depicted in Fig. 13. These zones are selected to have a higher probability to sever different lines with the two shots. Both the impacts created a visible crater in the respective target zones as shown in Fig. 13.

Both the shots do not perforate the IS-SP showing its capability of shielding the CubeSat internal electronics from the impact. The two impacts are detected by the sensor: after the first shot, 2 lines are severed while after the second one 4 other are cut by the impact.

Table 12
Sinusoidal load profile used in testing.

Frequency [Hz]	O-peak [g]
[5–70]	2.0
[70–125]	1.0

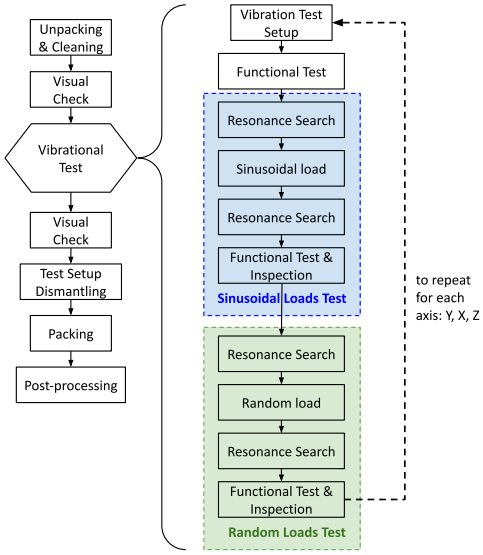

Fig. 14. Vibration Test sequence followed for the test campaign. The system is subjected to sinusoidal and then random loads along each reference axis, respectively. A resonance search is executed before and after every vibration step.

A visual inspection of the IS-DET confirmed that the severed lines correspond to the ones that the sensor detects as open.

4.3. Vibration test

A vibration test campaign is performed by means of an electrodynamic shaker to evaluate the structural response of the DUT during the launch and to assess its capability to withstand the applied loads. In the test campaign the shaker of the Centre of Studies and Activities for Space (CISAS) of Padova is used. The facility has a maximum force of 10 kN in the frequency range of 5–5000 Hz.

A sinusoidal vibration test and a random vibration test are performed for each axis (Fig. 1) of the DM of the IS-SA. In the DM the control electronics is in a breadboard configuration so, being not representative of the FM, it is not tested for vibration loads.

The aim of the vibration test was to confirm the capability of the IS-SA glued interface and their fixture system to the CubeSat to withstand the launch loads. The sinusoidal load profile and the Power Spectral Density (PSD) of the random load profile used for the test are shown in Fig. 9 (yellow line) and Table 12, respectively. The sinusoidal loads are considered at acceptance level according to [47]. The random load profile is equal to the GEVS [48] at acceptance level with an addiction of +3 dB from 100 Hz so that to consider possible amplifications.

The test procedure is outlined in Fig. 14. The DUT is mounted on a rigid aluminum interface. In order to test the DUT on each of the three axes, two different aluminum interfaces are used: one for the test on the Y and Z axes and one for the X axis. A triaxial piezoelectric accelerometer (model 356A32 by PCB Piezotronics) is used for measuring the response of the IS-SA to the loads. It is attached in the middle of the IS-DET and oriented according to the sensor reference frame. Another accelerometer equal to the former is positioned on the aluminum interface as a ground-truth of the applied loads. The performance parameters of the accelerometer are provided in Table 13. A monoaxial accelerometer of type 4507-B-001 is fixed to the armature of the facility to control the applied loads.

Table 13
Triaxial accelerometer performance and physical specifications.

Parameter	Value
Mass	5.4 g
Sensitivity ±10%	10.2 mV/(m/s^2)
Measurement range	± 491 m s^{-2}
Frequency Range (±5%)	1.0 to 4000 Hz
Transverse Sensitivity	≤ 5%

Table 14
DUT resonances.

Resonance [Hz]	Involved axes
640	X
870	X, Y, Z
1080	X, Z
1300	X, Y, Z
1690	Y, Z

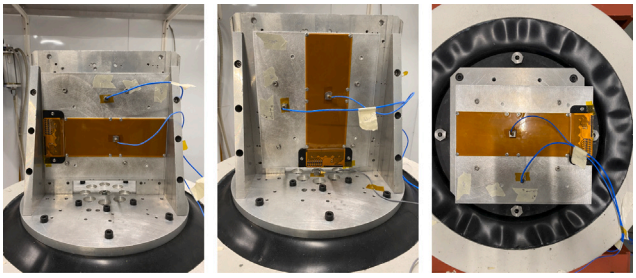

(a) (b) (c)

Fig. 15. Vibration Test setups: Y axis test setup (a), Z axis test setup (b), X axis test setup (c).

For the first vibration sequence, i.e. along the Y axis of the sensor, the DUT is fixed to the armature of the shaker as in Fig. 15(a). After a first functional test to collect the reference data of the lines statuses a resonance search is performed to determine the natural frequencies of the DUT. Subsequently, the sinusoidal loads and then the random loads are tested following the reference curves. Every vibration step is followed by a resonance search, a inspection and a functional test to verify the integrity and the functionality of the sensor. Then, the process is repeated for the other axes. Finally, the test setup is dismantled and packed.

No alarms were observed during the execution of the test procedure, confirming that the load applied to the DUT was consistent with the required profiles. To establish the pass/fail criteria related to the resonance search test, the ECSS-E-ST-10-03C Rev.1 [52] was consulted. No shifts in terms of frequency and amplitude out of the ranges ±5% and ±20%, respectively, were observed for resonances with an effective mass above 10% during the post-processing analysis of accelerometer data. The identified resonance peaks are listed in Table 14. The first natural frequency occurred at approximately 640 Hz (mono-axial mode), representing the only resonance with an effective mass exceeding 10% of the total DUT mass. Subsequently, triaxial resonance modes were detected at 870 Hz and 1300 Hz, while two bi-axial resonance modes were observed at 1080 Hz and 1690 Hz.

In conclusion, throughout the test, no anomalies were detected, and all pass/fail criteria were successfully met. Specifically, the sensor operated nominally during all functional tests performed. Additionally, no visible deformations or detachments were observed on the DUT.

5. Conclusions

In this study, a novel design of an impact sensor tailored for CubeSat applications is introduced. The sensor is capable of detecting impacts with sub-mm space debris up to 80 µm. Compared to existing literature, the presented sensor boasts low-power consumption while maintaining the necessary sensitivity to detect sub-mm impacts. Moreover, its resistive design, employing conductive lines arranged on a thin, flexible Kapton film, enables easy scaling and installation in a wide range of spacecrafts. However, its compactness and low power consumption render the sensor particularly suitable for implementation in CubeSat missions.

The analyses conducted to predict the number of impacts, thermal behaviour in orbit, and structural response during launch validate the feasibility of the design. Specifically, debris impact simulations show results with high uncertainties, demonstrating the low reliability of the current models to predict impacts with sub-millimeter space debris in LEO. Thermal simulations demonstrate the capability of the sensor to endure the in-orbit temperature during the mission. Structural analyses assess that the sensor can withstand the launch loads without failure.

Finally, the functional and vibration tests performed on the development model of the sensor demonstrate its capability to detect an impact, and that its sensitive assembly (IS-SA) can survive the vibration environment during launch. This way, the functionality of the sensor is demonstrated in a laboratory environment, allowing the achievement of a TRL of 4.

As future work, the Engineering Qualification Model (EQM) will be produced and it will undergo a full environmental test campaign.

CRediT authorship contribution statement

Samuele Enzo: Writing – original draft, Investigation, Data curation, Conceptualization. **Giacomo Battaglia:** Writing – original draft, Software, Investigation. **Federico Basana:** Writing – review & editing. **Francesca Filippini:** Writing – original draft. **Monica Mozzato:** Writing – original draft. **Federico Marin:** Writing – original draft. **Luca Lion:** Writing – review & editing. **Lorenzo Olivieri:** Writing – review & editing. **Carlo Bettanini:** Supervision. **Alessandro Francesconi:** Supervision.

Declaration of competing interest

The authors declare that they have no known competing financial interests or personal relationships that could have appeared to influence the work reported in this paper.

Acknowledgements

The authors thanks the ESA experts that are following the AlbaSat mission under the Fly Your Satellite! - Design Booster programme. In addition, the authors thanks the “Tiro a Segno Padova” for its precious support during the test at the shooting range of Padova.

References

[1] T. Maclay, D. Mcknight, Space environment management: Framing the objective and setting priorities for controlling orbital debris risk, J. Space Saf. Eng. 8 (1) (2021) 93–97.
[2] H.G. Lewis, G.G. Swinerd, R.J. Newland, The space debris environment: Future evolution, Aeronaut. J. 115 (1166) (2011) 241–247.
[3] D.J. Kessler, N.L. Johnson, J. Liou, M. Matney, The Kessler syndrome: Implications to future space operations, Adv. Astronaut. Sci. 137 (8) (2010) 2010.
[4] L. Olivieri, A. Francesconi, Large constellations assessment and optimization in LEO space debris environment, Adv. Space Res. 65 (1) (2020) 351–363.
[5] H. Lewis, J. Radtke, A. Rossi, J. Beck, M. Oswald, P. Anderson, B. Bastida Virgili, H. Krag, Sensitivity of the space debris environment to large constellations and small satellites, J. Br. Interplanet. Soc. 70 (2–4) (2017) 105–117.
[6] H.G. Lewis, B. Schwarz, S. George, H. Stokes, An assessment of CubeSat collision risk, in: Proceedings of the International Astronautical Conference, 2014.
[7] J. Radtke, E. Stoll, H. Lewis, B. Bastida Virgili, The impact of the increase in small satellite launch traffic on the long-term evolution of the space debris environment, in: Proceedings of the 7th European Conference on Space Debris, The European Space Agency (ESA), 2017.

[8] D.L. Oltrogge, I.A. Christensen, Space governance in the new space era, J. Space Saf. Eng. 7 (3) (2020) 432–438.
[9] C. Portelli, F. Alby, R. Crowther, U. Wirt, Space debris mitigation in France, Germany, Italy and United Kingdom, Adv. Space Res. 45 (8) (2010) 1035–1041.
[10] H. Stokes, Y. Akahoshi, C. Bonnal, R. Destefanis, Y. Gu, A. Kato, A. Kutomanov, A. LaCroix, S. Lemmens, A. Lohvynenko, et al., Evolution of ISO's space debris mitigation standards, J. Space Saf. Eng. 7 (3) (2020) 325–331.
[11] C. Bonnal, J.-M. Ruault, M.-C. Desjean, Active debris removal: Recent progress and current trends, Acta Astronaut. 85 (2013) 51–60.
[12] M. Shan, J. Guo, E. Gill, Review and comparison of active space debris capturing and removal methods, Prog. Aerosp. Sci. 80 (2016) 18–32.
[13] C.P. Mark, S. Kamath, Review of active space debris removal methods, Space Policy 47 (2019) 194–206.
[14] L. Olivieri, A. Valmorbida, G. Sarego, E. Lungavia, D. Vertuani, E.C. Lorenzini, Test of tethered deorbiting of space debris, Adv. Astronaut. Sci. Technol. 3 (2020) 115–124.
[15] J.L. Forshaw, G.S. Aglietti, N. Navarathinam, H. Kadhem, T. Salmon, A. Pisseloup, E. Joffre, T. Chabot, I. Retat, R. Axthelm, et al., RemoveDEBRIS: An in-orbit active debris removal demonstration mission, Acta Astronaut. 127 (2016) 448–463.
[16] R. Biesbroek, S. Aziz, A. Wolahan, S.-f. Cipolla, M. Richard-Noca, L. Piguet, The clearspace-1 mission: ESA and clearspace team up to remove debris, in: Proc. 8th Eur. Conf. Sp. Debris, 2021, pp. 1–3.
[17] D. McKnight, R. Witner, F. Letizia, S. Lemmens, L. Anselmo, C. Pardini, A. Rossi, C. Kunstadter, S. Kawamoto, V. Aslanov, et al., Identifying the 50 statistically-most-concerning derelict objects in LEO, Acta Astronaut. 181 (2021) 282–291.
[18] P. Ravi, C. Frueh, T. Schildknecht, Investigation of three recent Atlas V Centaur upper stage fragmentation events, in: 8th European Conference on Space Debris, vol. 8, 2021.
[19] L. Olivieri, C. Giacomuzzo, D.-J. Cristina, A. Francesconi, C. Camilla, et al., Fragments distribution prediction for ENVISAT catastrophic fragmentation, in: 8th European Conference on Space Debris, ESA/ESOC, 2021, pp. 1–12.
[20] N.L. Johnson, US space surveillance, Adv. Space Res. 13 (8) (1993) 5–20.
[21] P. Faucher, R. Peldszus, A. Gravier, Operational space surveillance and tracking in Europe, J. Space Saf. Eng. 7 (3) (2020) 420–425.
[22] J.A. Kennewell, B.-N. Vo, An overview of space situational awareness, in: Proceedings of the 16th International Conference on Information Fusion, IEEE, 2013, pp. 1029–1036.
[23] M. Polkowska, Space situational awareness (SSA) for providing safety and security in outer space: Implementation challenges for europe, Space Policy 51 (2020) 101347.
[24] J.V. Cabrera, S. Nag, D.D. Murakami, An initial analysis of automating conjunction assessment and collision avoidance planning in space traffic management, in: AAS/AIAA Space Flight Mechanics Meeting, (no. ARC-E-DAA-TN64689) 2019.
[25] J. Gonzalo Gòmez, C. Colombo, et al., Collision avoidance algorithms for space traffic management applications, in: International Astronautical Congress, IAC, 2020, pp. 1–8.
[26] N. Welty, M. Rudolph, F. Schäfer, J. Apeldoorn, R. Janovsky, Computational methodology to predict satellite system-level effects from impacts of untrackable space debris, Acta Astronaut. 88 (2013) 35–43.
[27] H. Krag, M. Serrano, V. Braun, P. Kuchynka, M. Catania, J. Siminski, M. Schimmerohn, X. Marc, D. Kuijper, I. Shurmer, et al., A 1 cm space debris impact onto the sentinel-1a solar array, Acta Astronaut. 137 (2017) 434–443.
[28] F. Alby, E. Lansard, T. Michal, Collision of cerise with space debris, in: Second European Conference on Space Debris, vol. 393, 1997, p. 589.
[29] T. Kelso, N. Parkhomenko, V. Shargorodsky, V. Vasiliev, V. Yurasov, A. Nazarenko, S. Tanygin, R. Hiles, What happened to blits? An analysis of the 2013 Jan 22 event, in: Proceedings of the Advanced Maui Optical and Space Surveillance Technologies Conference, vol. 4, 2013.
[30] A. Francesconi, C. Giacomuzzo, L. Olivieri, G. Sarego, A. Valmorbida, M. Duzzi, K.D. Bunte, E. Farahvashi, T. Cardone, D. de Wilde, Numerical simulations of hypervelocity collisions scenarios against a large satellite, Int. J. Impact Eng. 162 (2022) 104130.
[31] A. Nicholas c., T.T. Finne, C.M. Brown, J.M. Wolf, K.D. Marr, V.M. Kooi, N.O. Arelanno, I.J. Galysh, S.A. Budzien, LARADO on-orbit optical detection of lethal non-trackable debris progress update, in: 2nd Orbital Debris Conference, 2023, pp. 1–10.
[32] D.M. Malaspina, Z. Sternovsky, Debris and meteoroid environment sensor (DENTS): A unified instrument for in-situ detection of < 3 mm debris & meteoroids and characterization of the near-spacecraft environment following hypervelocity impacts, in: 2nd Orbital Debris Conference, 2023, pp. 1–10.
[33] M. Michel, H. Ceeh, J. Utzmann, S. Carli, G. Desroches, O. Croatto, G. Cirillo, M. Armbruster, S. Mangelsdorf, S. Christian, X. Oikonomidou, I. Biswas, C. Baweja, J. Siminkiski, T. Flohrer, S. Kraft, The space-based optical component (SBOC) instrument for passive optical in-situ detection of small space debris, in: 2nd Orbital Debris Conference, 2023, pp. 1–9.
[34] A. Moussi, G. Drolshagen, J. McDonnell, J.-C. Mandeville, A. Kearsley, H. Ludwig, Hypervelocity impacts on HST solar arrays and the debris and meteoroids population, Adv. Space Res. 35 (7) (2005) 1243–1253, http://dx.doi.org/10.1016/j.asr.2005.03.060.
[35] M. Nakamura, Y. Kitazawa, H. Matsumoto, O. Okudaira, T. Hanada, A. Sakurai, K. Funakoshi, T. Yasaka, S. Hasegawa, M. Kobayashi, Development of in-situ micro-debris measurement system, Adv. Space Res. 56 (3) (2015) 436–448, http://dx.doi.org/10.1016/j.asr.2015.04.009, Advances in Asteroid and Space Debris Science and Technology - Part 1.
[36] Japan Aerospace Exploration Agency (JAXA), Space debris monitor,
[37] J. Hamilton, J. Liou, P. Anz-Meador, B. Corsaro, F. Giovane, M. Matney, E. Christiansen, In-situ sub-millimeter space debris detection using CubeSats, Adv. Astronaut. Sci. 144 (2012).
[38] J. Kuitunen, G. Drolshagen, J. McDonnell, H. Svedhem, M. Leese, H. Mannermaa, M. Kaipiainen, V. Sipinen, DEBIE - first standard in-situ debris monitoring instrument, in: Proceedings of the 3rd European Conference on Space Debris, ESOC, Darmstadt, Universitat Politècnica de Catalunya, 2001.
[39] K. Gamble, H. Kjellberg, G. Lightsey, A. Wolf, R. Laufer, In-situ sub-millimeter space debris detection using CubeSats, Adv. Astronaut. Sci. 144 (2012).
[40] W. Bauer, O. Romberg, H. Krag, G.H. Visser, D. Digirolamo, M.F. Barschke, S. Montenegro, Debris in-situ impact detection by utillization of CubeSat solar panels, in: The 4S Symposium, Malta, 2016.
[41] F. Basana, L. Lion, L. Olivieri, F. Berra, L. Guglielmini, A. Stanco, A. Abbatecola, G. Battaglia, G. Bezze, M. Carrossa, S. Enzo, R. Lazzaro, M. Mozzato, L. Nuti, G. Stocco, A. Francesconi, AlbaSat: An educational satellite for a multi-objective mission in LEO, in: Proceedings of the 74th International Astronautical Congress, IAC, Baku, Azerbaijan, 2023.
[42] G. Battaglia, S. Enzo, G. Trevisanuto, S. Lopresti, F. Marin, G. Bezze, L. Olivieri, F. Basana, A. Francesconi, A CubeSat-sized in-situ space debris impact sensor, in: Proceedings of the 74th International Astronautical Congress, IAC, Baku, Azerbaijan, 2023.
[43] Mitigating in-space charging effects - a guideline, 2011.
[44] Q. Ouyang, W. Wang, Q. Fu, D. Dong, Atomic oxygen irradiation resistance of transparent conductive oxide thin films, Thin Solid Films 623 (2017) 31–39.
[45] V. Braun, A. Horstmann, S. Lemmens, C. Wiedemann, L. Böttcher, Recent developments in space debris environment modelling, verification and validation with MASTER, in: 8th European Conference on Space Debris, 2021.
[46] ECSS-E-HB-31-03A - Thermal Analysis Handbook, 2016.
[47] Small spacecraft mission service VEGA-c user's manual issue 1 – revision 0, 2020.
[48] General environmental verification standard (GEVS) for GSFC flight programs and projects, 2021.
[49] ECSS-E-ST-32-10C Rev.2 - Structural factors of safety for spaceflight hardware, 2019.
[50] CubeSat design specification (1U – 12U) REV 14.1, 2022.
[51] ECSS-E-HB-11A - Technology readiness level (TRL) guidelines, 2017.
[52] ECSS-E-ST-10-03C Rev.1 - Space engineering testing, 2022.